The 14th International Meeting on Fully Three-Dimensional Image Reconstruction in Radiology and Nuclear Medicine
June 2017, Xi'an

1

Theoretical Study of Benefit of Long Axial Field-of-View PET: Impact on Quantification Performance

Xuezhu Zhang, Ramsey D. Badawi, Simon R. Cherry and Jinyi Qi*

Abstract—We are building a 2-meter long PET scanner, called EXPLORER, that can provide high sensitivity and temporal resolution for total-body PET imaging. The aim of this study is to evaluate the improvement on quantification performance offered by the long axial field-of-view (FOV) of the EXPLORER. We use theoretical formulae based on the Fisher information matrix (FIM) of the penalized maximum likelihood image reconstruction to compute the contrast recovery coefficient (CRC) and the variance for region of interest (ROI) quantification. The CRC versus variance tradeoff curves were compared for a series of human PET scanners with a ring diameter of 83.5 cm and an axial FOV ranging from 22 cm to 220 cm. A series of mini-EXPLORER scanners with a ring diameter of 40 cm and axial FOV ranging from 11 cm to 110 cm was also examined and compared to the human scanners. A uniform cylinder (20 cm diameter and 220 cm long) was used to model the attenuation and background activity. The comparison showed that for imaging a single small ROI at the center of the axial FOV, the EXPLORER offers a 2.7-fold variance reduction over the 22-cm long scanner. For imaging an extended axial FOV of 110 cm, the EXPLORER provides a 30-fold variance reduction over the 22-cm long scanner and a 2~3 fold variance reduction over the 110-cm long scanner. These theoretical results clearly demonstrate the large possible improvement in image quality for extended FOV imaging and are consistent with our previous results obtained from reconstructions of Monte Carlo simulated human phantom data.

I. INTRODUCTION

Current PET scanners provide a limited axial field-of-view (FOV) (<30 cm) which restricts PET applications to regional imaging with low sensitivity and poor temporal resolution. The EXPLORER project aims to build a 2-meter long total-body human PET scanner [1], which will not only massively increase the sensitivity (up to a factor of 40-fold), but also provide superior temporal resolution for total-body dynamic imaging [2]–[4]. It will allow wide range of potential applications to be explored and afford opportunities in translational PET imaging currently unavailable to state-of-the-art clinical scanners. To date we have built a 45-cm long mini-EXPLORER scanner [5], which can perform total-body pre-clinical PET imaging in non-human primates and medium-size animals. In this work, we evaluate the improvement on quantification performance offered by the long axial FOV of the EXPLORER. Contrast recovery coefficient

The authors are with the Department of Biomedical Engineering and Department of Radiology, University of California, Davis, CA 95616 USA

(CRC) and variance of region of interest (ROI) quantification were analyzed theoretically and compared across a series of PET scanners with axial FOVs ranging from 22 cm to 220 cm. Performance of the mini-EXPLORER was also compared with the human EXPLORER scanner.

II. MATERIALS AND METHODS

A. Scanner configurations

We examined a series of human PET scanners with a range of axial FOVs. The ring diameter of the human scanners was fixed at 83.5 cm. Each detector ring is formed by 48 detector blocks (48B). Each detector block consists of a 13×13 array of $4\times4\times20$ mm^3 LSO crystals and has a dimension of 52 mm$\times$52 mm. Each PET scanner is made of multiple detector rings with a 4-mm axial gap between adjacent detector rings. In total we simulated 10 designs with 4, 8, 12, 16, 20, 24, 28, 32, 36 and 40 detector rings, respectively, which we refer to as 48B4R, 48B8R, ... , 48B36R, 48B40R in the following discussion. In addition, to compare the performance between the mini-EXPLORER scanner and human EXPLORER, we also simulated a series of designs with a ring diameter of 40 cm, formed by 24 detector modules (24B), with half the number of rings of the corresponding human scanner. We refer to them as 24B2R, 24B4R, ... , 24B18R, 24B20R, respectively.
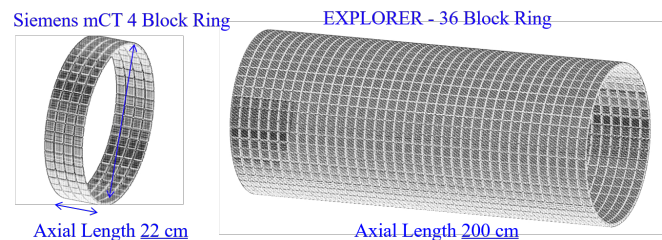

Fig. 1: Illustration of the simulated 4-ring scanner (48B4R) and 36-rings scanner (48B36R).

B. ROI quantification

We use the theoretical formulae derived for penalized likelihood image reconstruction [6]–[8] to compute the CRC and variance of ROI quantification. These formulae have

been verified extensively against Monte Carlo reconstructions. Here we briefly describe the results and refer readers to the references for more details.

For PET data that follow the Poisson likelihood function, the Fisher information matrix (FIM) is given by

$$\boldsymbol{F} = \boldsymbol{P}'\mathrm{diag}\left\{\frac{1}{\bar{y}_i}\right\}\boldsymbol{P} \qquad (1)$$

where $\boldsymbol{P}$ is the system matrix that models the probability of detecting an event from each image voxel in each line of response (LOR), $\bar{y}_i$ is the expected measurement at the ith LOR. The CRC and variance of an ROI can be approximated by

$$\mathrm{CRC} \approx= \frac{1}{|\boldsymbol{f}_I|}\boldsymbol{f}_I'[\boldsymbol{F}+\beta\boldsymbol{R}]^{-1}\boldsymbol{F}\boldsymbol{f}_I \qquad (2)$$

$$\mathrm{Var}_j(\hat{x}) = \boldsymbol{f}_I'[\boldsymbol{F}+\beta\boldsymbol{R}]^{-1}\boldsymbol{F}[\boldsymbol{F}+\beta\boldsymbol{R}]^{-1}\boldsymbol{f}_I \qquad (3)$$

where β is the regularization parameter in the penalized likelihood reconstruction, $\boldsymbol{R}$ is the second-order derivative of the penalty function, and $\boldsymbol{f}_I$ is the ROI indicator function. $|\boldsymbol{f}_I|$ denotes the number of voxels in the ROI.

Direct inversion of the Fisher information matrix is difficult because of its huge dimension. Fortunately, for a small ROI, the above equations can be evaluated by using the locally shift-invariant approximation and fast Fourier transform [7]. The formulae become

$$\mathrm{crc}_j \approx \frac{1}{N|\boldsymbol{f}_I|}\sum_{i=0}^{N-1}\frac{\lambda_i|\gamma_i|^2}{\lambda_i+\beta\mu_i} \qquad (4)$$

$$\mathrm{var}_j \approx \frac{1}{N}\sum_{i=0}^{N-1}\frac{\lambda_i|\gamma_i|^2}{(\lambda_i+\beta\mu_i)^2} \qquad (5)$$

where λ and μ are the Fourier transform of the column of $\boldsymbol{F}$ and $\boldsymbol{R}$ corresponding to the ROI location, respectively, and γ is the Fourier transform of $\boldsymbol{f}_I$.

C. Evaluation studies

We first computed one column of the Fisher information matrix corresponding to the voxel at the FOV center for all scanner configurations. A uniform cylinder (20-cm diameter and 220-cm long) was used to model the attenuation and background activity, i.e., for the calculation of $\bar{y}_i$. The system matrix was computed using a multi-ray-tracing projector that divides each detector crystal into $4\times4\times20$ sub-elements and traces all the possible lines connecting the elements of two detectors. The image dimension was $135 \times 135 \times 1119$ with $2\times2\times2$ mm^3 voxels.

To compare the quantification performance, we examined two scenarios. The first one is to image a single ROI at the center of the FOV of each scanner. This gives the best performance of each scanner for imaging a fixed point with one bed position. The second scenario is to image an extended axial FOV of 110 cm, which corresponding to a typical whole-body PET scan FOV. For scanners with a shorter axial FOV, multiple bed positions with 50% axial overlap are used. Specifically, the number of bed positions

are 11 for 48B4R, 6 for 48B8R, 3 for 48B20R, and 1 for 48B40R. All of these are designed to provide a relatively uniform sensitivity across the 110 cm axial FOV. The total scan time is kept the same. In both imaging scenarios, we compare the CRC versus variance curve for quantifying a 10-mm ROI.

III. RESULTS

A. 48B versus 24B scanners

Fig. 2 shows the peak value of Fisher information matrix calculated for the point at the FOV center of different scanners. We can see that the 48B human scanners and their 24B primate counterparts possess very similar performance because they have almost the same acceptance angle with similar geometric sensitivity. The minor difference between the 48B40R and 24B20R scanners are because they use the same detector blocks and are not exactly proportional. The Fisher information achieved using TOF resolution of 320 ps exceeded that at 500 ps and nonTOF, indicating that better performance can be achieved by higher timing resolution.
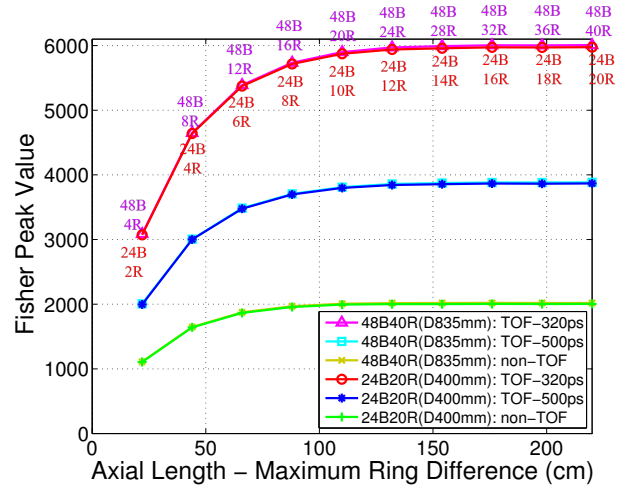

Fig. 2: Fisher information peak value at the FOV center location of scanner with different axial length (22 cm to 220 cm).

B. Single point imaging

Fig. 3 shows the comparison of sensitivity of a point source in air along the center axis of the scanners with 4, 8, 20 and 40 rings. All the curves are scaled to the peak sensitivity of 48B4R. We can see that the 2-m long EXPLORER offers a ~4.3-fold increase in the peak sensitivity than the 4-ring scanner. The 1-m long 48B20R scanner offers a ~3.5-fold increase in the peak sensitivity, but the sensitivity reduces rapidly away from center.

The theoretical CRC and variance curves of the 10-mm ROI are shown in Fig. 4. The TOF resolution is 500 ps. We can see that the 48B16R~48B40R scanners have similar performance and all outperforms the 48B4R~48B12R. For

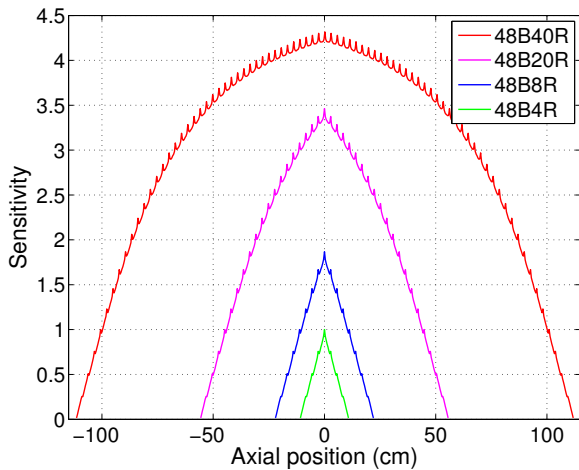Fig. 3: Sensitivity of the scanners with 4, 8, 20, 40 rings (48B4R∼48B40R) (scaled to that of 48B4R).

Fig. 5: Theoretical variance reduction ratio of a 10-mm ROI at the FOV center of scanners with 8∼40 rings (48B8R∼48B40R) over the 4-ring scanner(48B4R).

an easier comparison, we plot the variance reduction ratio of different scanners over 48B4R as a function of CRC in Fig. 5, which clearly shows the differences between the scanners. We can see a 2.6∼2.8-fold variance reduction from the scanners with an axial FOV longer than 110 cm. The gains remain relatively flat in the CRC range of 0.1∼0.6 and decrease at higher CRC values. The decrease is due to the fact that LORs with larger ring difference suffer more crystal penetration effect and hence have lower intrinsic resolution than LORs with less ring difference. The fact that 48B20R and 48B40R achieve similar performance also indicates that the image quality over the middle 110-cm axial FOV of the 40-ring scanner is fairly uniform, which offers a unique advantage for total-body imaging.
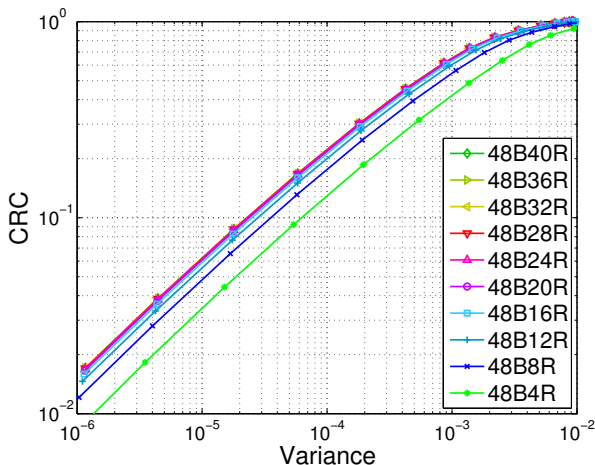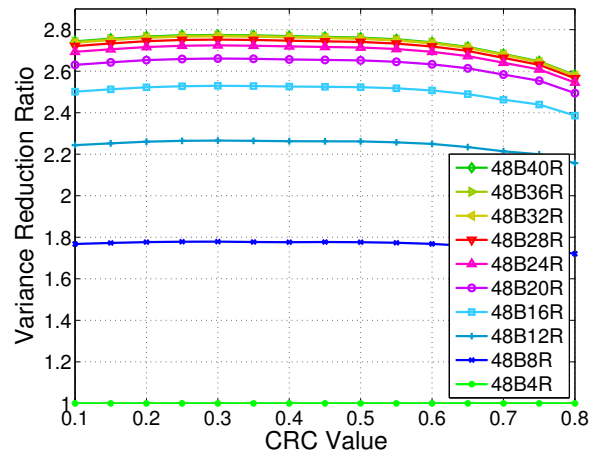
an extended axial FOV of 110 cm. All the curves are normalized to the maximum sensitivity of the 4-ring scanner (48B4R). All scanners provide a relatively uniform sensitivity across the 110-cm axial FOV. Overall, the EXPLORER (48B40R) offers ∼40-fold increase in sensitivity over the 4-ring scanner (48B4R), and ∼15 and ∼3-fold increase in sensitivity over the 8-ring and 20-ring scanners, respectively. There are noticeable variations in the 48B20R sensitivity profile, because its axial sensitivity does not strictly follow a triangular shape. For a comprehensive comparison, we evaluated the quantification performance for ROI located at both the maximum and minimum sensitivity inside the 110-cm axial FOV.
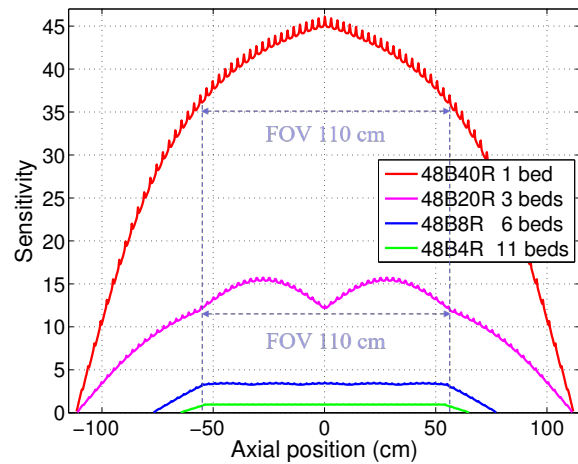

Fig. 4: Theoretical CRC vs. variance of a 10-mm ROI at the FOV center (TOF 500 ps).

Fig. 6: Sensitivity of multiple-bed protocol (50% overlap) covering 110 cm axial FOV using the scanners with 4, 8, 20, 40 rings (48B4R∼48B40R).

C. Extended FOV imaging

Fig. 6 shows the comparison of sensitivity along the axial axis provided by the different scanners for imaging

Fig. 7 shows the theoretical CRC vs. variance of the 4-scanners for imaging the extended axial FOV. We can see almost overlapping curves for the 48B40R at center and 55-cm axial offset, indicating that the 2-meter long scanners can

provide very uniform image quality over the central 110-cm of the axial FOV. However, the best and worse CRC vs. variance curves of the 48B20R with 3 beds scan have large differences and both are substantially worse than those of the 48B40R scanner.

Fig. 8 plots the variance reduction factor of different scanners over the 4-ring scanner (48B4R). We can clearly see that for imaging a 110-cm axial FOV, the 48B40R has a $\sim$30-fold gain over the 48B4R, 8$\sim$10-fold gain over the 48B8R, and 2$\sim$3-fold gain over the 48B20R.
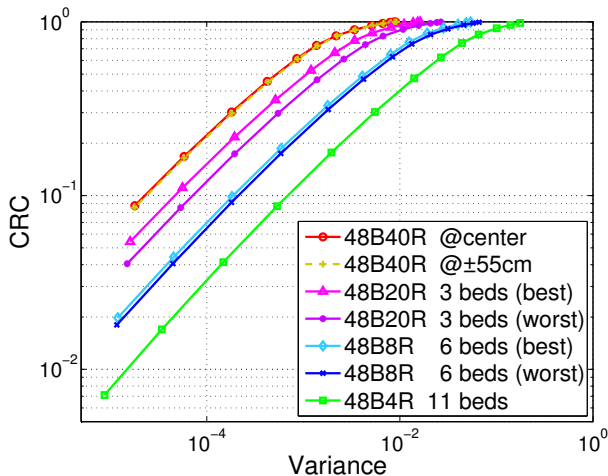

Fig. 7: Theoretical CRC vs. variance of a 10-mm ROI in the 110-cm axial FOV by multiple-bed protocol using scanners with 4, 8, 20, 40 rings (TOF 500 ps).
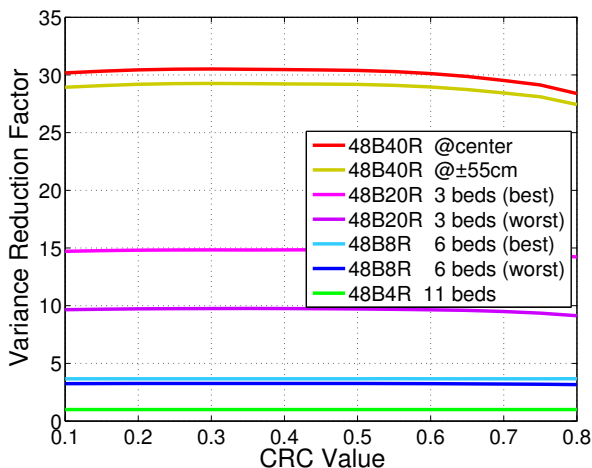

Fig. 8: Variance reduction factor for the 10-mm ROI in the 110-cm axial FOV of different scanners over the 4-ring scanner (48B4R).

IV. CONCLUSION

In this paper, we used theoretical analysis to evaluate the improvement on PET quantification performance achieved by the EXPLORER scanner with an extended axial FOV.

The comparison results show that the EXPLORER scanner offers a 2.8-fold variance reduction for imaging a fixed point and 30-fold variance reduction for imaging an extended 110-cm axial FOV over the 4-ring scanner. The EXPLORER scanner also offers a 2$\sim$3-fold improvement over a 1-m long scanner for the extended axial FOV imaging. These theoretical results are congruent with our previous Monte Carlo simulation studies comparing the EXPLORER scanner with a 4-ring scanner, where we obtained a variance reduction factor of 25 [4]. The slight difference could be either due to the fact that the theoretical analysis in this paper does not include any scattered and random events or might be caused by statistical variation in the Monte Carlo simulation. Our future work will include further validation using experimental data.

REFERENCES

[1] EXPLORER project website: http://explorer.ucdavis.edu/
[2] Zhang X, Zhou J, Wang G, Poon J K, Cherry S R, Badawi R D and Qi J 2014 *J. Nucl. Med.* 55 (Supplement 1):269
[3] Zhang X, Berg E, Bec J, Judenhofer M S, Kapusta M, Schmand M, Casey M, Badawi R D, Cherry S R and Qi J 2017 First Pre-Clinical Study of Total-Body Dynamic PET Imaging using the mini-EXPLORER Scanner *SNMMI Annual Meeting* submitted
[4] Zhang X, Zhou J, Cherry S R, Badawi R D and Qi J 2017 Quantitative Image Reconstruction for Total-Body PET Imaging Using the 2-meter Long EXPLORER Scanner *Phys Med Biol.* Accepted
[5] Berg E, Zhang X, Bec J, Judenhofer M S, Peng Q, Kapusta M, Schmand M, Casey M, Qi J, Badawi R D and Cherry S R 2016 Evaluation of a long axial field-of-view PET scanner for non-human primates *2016 IEEE NSS-MIC* MO6-4
[6] Qi J and Leahy R M 1999 A theoretical study of the contrast recovery and variance of MAP reconstructions from PET data *IEEE Trans. Med. Imaging* 18 293-305
[7] Qi J and Leahy R M 2000 Resolution and noise properties of MAP reconstruction for fully 3D PET *IEEE Trans. Med. Imaging* 19 493-506
[8] Qi J and Huesman R H 2006 Theoretical Study of Penalized-Likelihood Image Reconstruction for Region of Interest Quantification *IEEE Trans. Med. Imaging* 25 640-648